Acta Acustica united with Acustica
Vol. 101 (2015) 760 – 774

DOI 10.3813/AAA.918871

Using Mode Matching Methods and Edge Diffraction in Horn Loudspeaker Simulation

Bjørn Kolbrek, U. Peter Svensson
Acoustics Research Centre, Department of Electronics and Telecomunications NTNU–Norwegian University of Science and Technology, Trondheim, Norway. [Bjorn.Kolbrek, Peter.Svensson]@iet.ntnu.no

Summary
A method for simulating an expanding duct, like a horn, by mode matching techniques is described. For a horn in an infinite baffle, the modal radiation impedance and radiated pressure can be found from known relations. For a horn equipped with a small baffle or flange, however, diffraction from the edges has to be taken into account. This paper investigates how an edge diffraction term can be included, and its effect on the throat and radiation impedances and radiated pressure. Measurement results are presented, and are shown to be in good agreement with the simulations, both for a horn in a large baffle, and for a horn with a small flange.

PACS no. 42.20.Mv, 43.38.Ja, 42.20.Ks

1. Introduction

When Webster published his famous paper on horns in 1919 [1], he was mainly concerned with the throat impedance, or loading properties, of the horn. The horn equation he presented, which is commonly known as Webster's equation[1], is one-dimensional, and can only predict pressure and velocity averaged over the assumed wave front surfaces in the horn.

For wind instruments, where radiation directivity is of minor importance, there has been much research into one-dimensional models for predicting their resonance frequencies [3, 4, 5]. The use of spherical, or even oblate elipsoidal, wavefronts have been used, together with a proper choice of radiation impedance model, to improve accuracy [6, 7, 8]. A similar approach has also been used to model horn loudspeakers [9].

But as has been pointed out by several authors [10, 11], one-dimensional horn theory is not able to predict the sound field radiated by a general horn, as the velocity distribution at the horn mouth is unknown. Consequently, the design of horn loudspeakers have to a large extent been based on experience, geometrical approaches [12], or Finite or Boundary Element Analysis [13, 14, 15].

By instead setting up the three-dimensional wave equation in a coordinate system where the wave equation is separable, and letting the horn walls follow the coordinate surfaces, it is for certain cases possible to find analytical solutions. These solutions will include higher order modes of propagation, and one is therefore able to predict the sound field inside the horn. There are, however, only eleven coordinate systems where the wave equation is separable, and very few of them have surfaces that give useful horn contours [10]. Furthermore, if analytical solutions are to be found for radiation from finite horns, one is restricted to enclosures that also follow the coordinate surfaces. For instance, it would be possible to find an analytical solution for a conical horn mounted in a sphere, but not for the same horn mounted in a rectangular box. Analysis of arbitrary geometries is therefore not possible.

A solution to this problem is to divide the horn into small, straight sections that each have analytical solutions, and then to match the sound fields at the interfaces, or discontinuities, between the sections. The cross sectional shape is still restricted, but now the axial shape of the horn can be arbitrary. This mode-matching approach was probably first implemented by Alfredson [16], who used an iterative technique. Alfredson used the method to compute the sound field radiated from an axisymmetric exponential horn.

Shindo *et al.* [17] and Schuhmacher and Rasmussen [18] simulated rectangular horns by a multimodal method, in which the amplitudes of the propagating and reflected waves in each section were found by solving a linear system of equations. This method has numerical challenges when dealing with evanescent waves, leading Shindo *et al.* to use the Boundary Element Method in the narrow parts of the horn.

Pagneux *et al.* [19] describe both a discrete model, a version of the discrete model carried to the limit of infinitesimal segment length, and a purely continuous model. The discrete model is also used by Kemp [20], and will be described in detail in the next section. Amir *et al.* [21] have verified experimentally and numerically that the discrete

Received 02 December 2014,
accepted 19 February 2015.

[1] Although the equation in question was derived and discussed by Bernoulli, Lagrange and Euler [2].

model carried to the limit is able to predict both the sound field inside the horn, and the input impedance of the horn. Kemp has also demonstrated that the discrete model is able to predict the input impedance of wind instruments with good accuracy. In both these studies, the horn was assumed mounted in an infinite baffle.

Similar to the one-dimensional horn models, the mode-matching models also require a good model for the radiation impedance. Fortunately, the dependence of the radiation impedance on the shape of the horn, as discussed in [7], is now expressed by coupling between pressure and velocity modes. Now the radiation impedance model can be selected based only on the cross-sectional shape of the horn mouth, and possibly other external influences, like diffraction and reflections.

In this paper, the discrete mode-matching method described by Pagneux and Kemp will be applied to the simulation of rectangular loudspeaker horns. For horn loudspeakers, accurate prediction of the radiated sound field is at least as important as the throat impedance, and it will be demonstrated that the method is able to predict the sound field outside the horn as well. By including edge diffraction, a significant improvement in the predicted results, for both throat impedance and radiated pressure, can be found for horns mounted in finite baffles.

2. Theory

The Mode Matching Method (MMM) is based on describing the sound field in connected duct sections of different cross sections by a weighted sum of eigenfunctions appropriate for the coordinate system used [20, 22, 23]. In a rectangular duct, modes are denoted (n_x, n_y), and there will be n_x by n_y nodal lines; $(n_x, n_y) = (0, 0)$ representing the plane wave mode.

A time harmonic factor of $e^{j\omega t}$ is implicitly assumed throughout the paper.

Along the duct, assuming propagation in the z direction, the pressure can be expressed as a sum of all the modes,

$$p(x, y, z) = \sum_{n=0}^{\infty} P_n(z)\psi_n(x, y), \tag{1}$$

where P_n is the pressure profile along the tube, and ψ_n is the pressure profile in the (x, y) plane. Here n is used as a short hand index for n_x, n_y, and the modes are sorted in increasing order, see Table I.

It is advantageous to separate ψ_n into two parts, one dependent on x, and the other on y,

$$\psi_n = \phi_{n_x}\sigma_{n_y}. \tag{2}$$

In a quarter symmetric ducts having hard wall boundary conditions, width $2a$ and height $2b$, the mode functions in Equation (2), are [23]

$$\phi_{n_x} = \begin{cases} 1: & n_x = 0 \\ \sqrt{2}\cos\left(n_x\pi x/a\right): & n_x > 0 \end{cases} \tag{3}$$

Table I. Mode pairs sorted in increasing order.

n	(n_x, n_y)	n	(n_x, n_y)
1	(0,0)	9	(2,2)
2	(0,1)	10	(0,3)
3	(1,0)	11	(3,0)
4	(1,1)	12	(1,3)
5	(0,2)	13	(3,1)
6	(2,0)	14	(2,3)
7	(1,2)	15	(3,2)
8	(2,1)	16	(3,3)

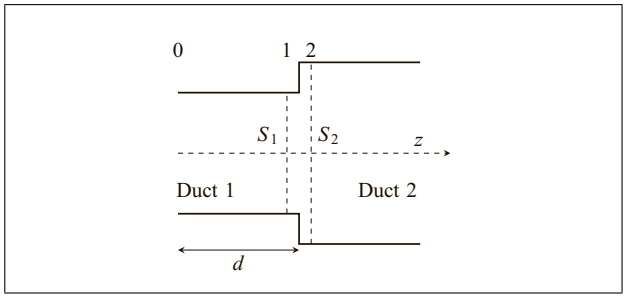

Figure 1. Two ducts joined by a discontinuity.

$$\sigma_{n_y} = \begin{cases} 1: & n_y = 0 \\ \sqrt{2}\cos\left(n_y\pi y/b\right): & n_y > 0. \end{cases} \tag{4}$$

In the z-direction, the pressure can be expressed as

$$P_n(z) = A_n e^{-jk_n z} + B_n e^{jk_n z}, \tag{5}$$

where

$$k_n = \begin{cases} -\sqrt{k^2 - \alpha_n^2}: & k^2 < \alpha_n^2 \\ \sqrt{k^2 - \alpha_n^2}: & k^2 > \alpha_n^2 \end{cases} \tag{6}$$

is the axial wavenumber of the nth mode pair, and k is the free space wavenumber. The eigenvalues α_n are

$$\alpha_n = \sqrt{\left(\frac{n_x\pi}{a}\right)^2 + \left(\frac{n_y\pi}{b}\right)^2}. \tag{7}$$

We can see that the axial wavenumber, k_n, will for certain values of α_n^2 be imaginary, and the propagation in the z direction will be evanescent (exponentially damped). The sign of the root is chosen to make the exponent in Equation (6), real and negative when k_n for $k^2 < \alpha_n^2$ is inserted into Equation (5). The wavenumber where k_n becomes real is called the cut-off (or sometimes cut-on) wavenumber of the corresponding mode.

When the wave propagates across a discontinuity (see Figure 1), there must be continuity of pressure and velocity right before (at position 1) and right after the discontinuity (at position 2). But the nth mode in duct 1 will not match the nth mode in duct 2, so the pressure field in duct 2 must be made up of a new sum of modes. Every mode in duct 1 excites a series of modes in duct 2, and this is known as modal coupling or mode conversion.

If $\vec{P}^{(1)}$ is the vector of modal pressure amplitudes at position 1, and $\vec{P}^{(2)}$ is the vector of modal pressure amplitudes at position 2, the vectors are related by a matrix F so that

$$\vec{P}^{(1)} = F\vec{P}^{(2)}, \tag{8}$$

where the matrix elements are computed by integrating over the area S_1 of duct 1,

$$F_{nm} = \frac{1}{S_1}\int_{S_1} \psi_n^{(1)}\psi_m^{(2)}\,\mathrm{d}S. \tag{9}$$

$\psi_n^{(1)}$ gives the mode shapes in duct 1, and $\psi_m^{(2)}$ gives the mode shapes in duct 2. This relation holds if $a_1 < a_2$, where a_1 and a_2 are the half-widths of the two ducts (and correspondingly for the half-heights $b_1$and b_2).

A corresponding relation exists for the volume velocity[2]:

$$\vec{U}^{(2)} = F^T\vec{U}^{(1)}. \tag{10}$$

If $a_1 > a_2$, and $b_1 > b_2$, the relations are

$$\vec{P}^{(2)} = V\vec{P}^{(1)}, \tag{11}$$
$$\vec{U}^{(1)} = V^T\vec{U}^{(2)}, \tag{12}$$

where the matrix elements are computed by integrating over the area S_2 of duct 2,

$$V_{nm} = \frac{1}{S_2}\int_{S_2} \psi_n^{(2)}\psi_m^{(1)}\,\mathrm{d}S. \tag{13}$$

For a rectangular duct, it is most convenient to express Equation (9) as an *element-wise* multiplication of two terms,

$$\begin{aligned} F_{nm}(\beta_x,\beta_y) &= \frac{1}{S_1}\int_{S_1} \psi_n^{(1)}\psi_m^{(2)}\,\mathrm{d}S \\ &= \frac{1}{2a_1}\int_{-a_1}^{a_1} \phi_{n_x}^{(1)}\phi_{m_x}^{(2)}\,\mathrm{d}x \frac{1}{2b_1}\int_{-b_1}^{b_1} \sigma_{n_y}^{(1)}\sigma_{m_y}^{(2)}\,\mathrm{d}y \\ &= X_{n_xm_x}Y_{n_ym_y}, \end{aligned} \tag{14}$$

where $\beta_x = a_1/a_2$ and $\beta_y = b_1/b_2$, and

$$X_{n_xm_x} = \begin{cases} 1: & n_x = m_x = 0, \\ \sqrt{2}\mathrm{sinc}\left(m_x\pi\beta_x\right): & n_x = 0,\ m_x > 0, \\ 2\mathrm{sinc}\left(A\right)\frac{m_x\beta_x}{m_x\beta_x+n_x}: & n_x > 0 \end{cases} \tag{15}$$

where

$$A = \pi(m_x\beta_x - n_x) \tag{16}$$

and

$$Y_{n_ym_y} = \begin{cases} 1: & n_y = m_y = 0, \\ \sqrt{2}\mathrm{sinc}\left(m_y\pi\beta_y\right): & n_y = 0,\ m_y > 0, \\ 2\mathrm{sinc}\left(B\right)\frac{m_y\beta_y}{m_y\beta_y+n_y}: & n_y > 0 \end{cases} \tag{17}$$

where

$$B = \pi(m_y\beta_y - n_y). \tag{18}$$

The V matrix then becomes

$$V_{nm} = F_{nm}(1/\beta_x,\ 1/\beta_y). \tag{19}$$

If the duct expands in one direction, and contracts in the other, the coupling matrix is split into two matrices that are subsequently multiplied, corresponding to two discontinuities directly following each other without any distance between them [24]. As an example, the first discontinuity expands in the x-direction and is constant in the y-direction, while the second discontinuity contracts in the y-direction and is constant in the x-direction. The first coupling matrix will be of the F-type, while the second will be of the V-type.

Pressure and volume velocity are related through the modal impedances, which can be expressed as

$$P_n = \sum_{m=0}^{\infty} Z_{nm}U_m. \tag{20}$$

This relation can be used to express how the modal impedances are coupled across the discontinuities,

$$Z^{(1)} = FZ^{(2)}F^T,\ S_1 < S_2, \tag{21}$$
$$Z^{(1)} = V^{-1}Z^{(2)}(V^T)^{-1},\ S_1 > S_2. \tag{22}$$

For propagation along a uniform duct, terminated by an impedance $Z^{(1)}$, the input impedance $Z^{(0)}$ can be found from the relation [20, corrected version] [3]:

$$\begin{aligned} Z^{(0)} &= (\mathrm{j}D_3)^{-1}Z_c - D_2^{-1}Z_c \\ &\quad\cdot\left(Z^{(1)} + \left(\mathrm{j}D_3\right)^{-1}Z_c\right)^{-1}D_2^{-1}Z_c. \end{aligned} \tag{23}$$

The extra matrices are defined as

$$D_2(n,m) = \begin{cases} \mathrm{j}\sin(k_nd): & n = m \\ 0: & n \neq m \end{cases} \tag{24}$$

$$D_3(n,m) = \begin{cases} \tan(k_nd): & n = m \\ 0: & n \neq m \end{cases} \tag{25}$$

$$Z_c(n,m) = \begin{cases} k\rho c/k_nS: & n = m \\ 0: & n \neq m \end{cases} \tag{26}$$

[2] Strictly speaking, only the first (plane wave) term in $\vec{U}$ can rightly be called the volume velocity. However, since the $\vec{U}$ vector can be expressed as $S\vec{u}$, where $\vec{u}$ is a vector of particle velocity mode amplitudes, we will refer to the entire $\vec{U}$ vector as the volume velocity.

[3] The corrected version of the thesis can be downloaded from `http://www.kempacoustics.com/thesis/index.html`

where d is the length of the duct as in Figure 1, and S is the cross-sectional area.

By using these relations, the impedance at the throat of the horn, the so-called throat impedance Z_{th}, can be found, given an impedance at the mouth of the horn.

Volume velocity is propagated along the duct as

$$\vec{U}^{(1)} = \left(-D_2 Z_c^{-1}\left(Z^{(0)} - Z_c\right) + E\right)\vec{U}^{(0)}, \qquad (27)$$

where the extra matrix is

$$E(n,m) = \begin{cases} \mathrm{e}^{-\mathrm{j}k_n d}: & n = m \\ 0: & n \neq m \end{cases}. \qquad (28)$$

Together with (10), (27) can be used to calculate the volume velocity mode amplitudes at the mouth of the horn, given the volume velocity amplitudes at the throat.

The traditional method to do this is outlined in [20], and is summarized as follows:

1. Calculate the impedance matrices at all points in the horn, starting from the mouth, using equations (21) or (22), and (23).
2. Excite the throat end with a given vector of volume velocity amplitudes, and propagate it to the mouth using equations (27), and (10) or (12).

This procedure requires storage of a large number of impedance matrices per frequency, one for each end of each duct element, which can be prohibitive if many modes and many duct elements are used. In addition, step 2 above must be repeated for each new throat velocity distribution.

However, inspection of Equations (27) and (10) shows that both are matrix-vector multiplications. Therefore, a single matrix for the entire horn, relating mouth volume velocity to throat volume velocity, can be found by multiplying together the matrices from these equations. What is more, this matrix can be built up from either end of the horn. The result is that the volume velocity transfer matrix can be built up simultaneously with the impedance matrix, from the mouth through to the throat, without storing the impedance values through the horn. This will result in a significant saving of computer memory. The fact that the diagonal matrices D_2 and Z_c only have to be calculated once per frequency and position will also reduce the computation time slightly. The revised procedure will then be:

1. Start with mouth impedance $Z^{(N)} = Z_{rad}$ (the radiation impedance) and volume velocity transfer matrix $\mathbb{U}^{(N,N)} = \boldsymbol{I}$.
2. For a straight duct element between positions $n-1$ and n, calculate $Z^{(n-1)}$ from Equation (23) and $Z^{(n)}$.
3. Calculate

$$\boldsymbol{M}^{(n-1,n)} = \left(-D_2 Z_c^{-1}\left(Z^{(n-1)} - Z_c\right) + E\right)$$

and

$$\mathbb{U}^{(n-1,N)} = \mathbb{U}^{(n,N)} \times \boldsymbol{M}^{(n-1,n)}.$$

4. For a discontinuity between positions $m-1$ and m, calculate $Z^{(m-1)}$ from Equation (21) and $Z^{(m)}$.
5. Calculate

$$\mathbb{U}^{(m-1,N)} = \mathbb{U}^{(m,N)} \times F^{T(m-1,m)}$$

from Equation (10) and $Z^{(m)}$.

More detailed derivations and information on how to implement the method in practice, can be found in [19, 20, 24].

2.1. Radiated Pressure

From a throat volume velocity vector $\vec{U}^{(1)}$ and the volume velocity transfer matrix $\mathbb{U}^{(1,N)}$, the mouth volume velocity mode amplitude vector $\vec{U}^{(N)}$ can be found as $\vec{U}^{(N)} = \mathbb{U}^{(1,N)}\vec{U}^{(1)}$. From this, the radiated pressure, p_{IB},can be calculated using a multimodal variant of the Rayleigh integral over the mouth area S,

$$p_{IB}(\mathbf{x}) = \frac{\mathrm{j}\omega\rho}{2\pi S}\int_S \sum_{m=0}^{\infty} \psi_m(x_0, y_0) U_m^{(N)} \frac{\mathrm{e}^{-\mathrm{j}kr}}{r}\,\mathrm{d}S_0, \qquad (29)$$

where $\mathbf{x} = (x, y, z)$ and

$$r = \sqrt{(x-x_0)^2 + (y-y_0)^2 + z^2}.$$

This expression is valid for the case of an infinite baffle, as indicated by the subscript IB for p.

2.2. Radiation impedance

The radiation impedance at the mouth end of the horn needs to be known in order to specify the boundary conditions at this end of the horn [19]. In general, the mechanical radiation impedance is defined as the area integral of the specific radiation impecance $p/v_{\mathbf{n}}$, where $v_{\mathbf{n}}$ is the normal surface velocity.[23]. The acoustic radiation impedance, Z_{rad}, for a surface S in an infinite baffle, is thus defined as

$$Z_{rad} = \frac{\mathrm{j}\omega\rho}{2\pi S^2}\int_S\int_S \frac{\mathrm{e}^{-\mathrm{j}kh}}{h}\,\mathrm{d}S_0\,\mathrm{d}S, \qquad (30)$$

where $h = \sqrt{(x-x_0)^2 + (y-y_0)^2}$.

In the multimodal case, the radiation impedance for a given velocity distribution is more complicated. Now, the radiation impedance must be expressed as [25]

$$Z_{rad} = \frac{W}{S^2\left\langle |v_{\mathbf{n}}|^2\right\rangle}, \qquad (31)$$

where $\left\langle |v_{\mathbf{n}}|^2\right\rangle = \frac{1}{S}\int_S v_{\mathbf{n}} v_{\mathbf{n}}^* dS$ is the mean square normal velocity, and $W = \int_S p v_{\mathbf{n}}^* dS$ is the radiated power. However, this is not a formulation that can be used directly with the MMM. What we need is a relation between each pressure mode and each velocity mode, so that the radiation impedance can be described as a matrix in the form of Equation (20). By combining Equation (1) with the orthogonality relation [20]

$$\int_S \psi_m \psi_n\,\mathrm{d}S = S\delta_{mn},$$

we can find the amplitude of the nth pressure mode as

$$P_n = \frac{1}{S}\int_S p(x, y, 0)\psi_n(x, y)\,\mathrm{d}S. \tag{32}$$

By substituting Equation (29) into Equation (32), we can find the amplitude of the nth pressure mode due to all velocity modes as

$$P_n = \frac{\mathrm{j}\omega\rho}{2\pi S^2}\sum_{m=0}^{\infty} U_m \int_S\int_S \frac{\mathrm{e}^{-\mathrm{j}kh}}{h} \cdot \psi_m(x_0, y_0)\,\psi_n(x, y)\,\mathrm{d}S_0\,\mathrm{d}S. \tag{33}$$

The factor $2\mathrm{e}^{-\mathrm{j}kh}/h$ in Equation (33) is the infinite-baffle Green's function, but other Green's functions can be inserted instead, if the surroundings are not represented by an infinite baffle. So, for the general case,

$$P_n = \frac{\mathrm{j}\omega\rho}{4\pi S^2}\sum_{m=0}^{\infty} U_m \int_S\int_S G(\mathbf{x}|\mathbf{x}_0) \cdot \psi_m(x_0, y_0)\,\psi_n(x, y)\,\mathrm{d}S_0\,\mathrm{d}S, \tag{34}$$

where $\mathbf{x}_0 = (x_0, y_0)$.

Comparing Equation (20) to Equation (34), we see that we can express the elements of the Z_{rad} as

$$Z_{mn} = \frac{\mathrm{j}\omega\rho}{4\pi S^2}\int_S\int_S G(\mathbf{x}|\mathbf{x}_0) \cdot \psi_m(x_0, y_0)\,\psi_n(x, y)\,\mathrm{d}S_0\,\mathrm{d}S. \tag{35}$$

In the case of an infinite baffle, the originally quadruple integral of Equation (35) can be simplified in various ways, depending on the mode functions and the coordinate system used. For details, see Zorumski [26] for a circular duct, and Kemp for rectangular ducts with symmetric [20] and asymmetric [27] modes. The symmetric mode case has been used in the calculations in this paper.

For rectangular ducts, Equation (35) reduces to a double integral, but the computational load is still large, especially if many modes are required. 16 modes in each direction result in a 256×256 matrix per frequency, and even though the matrix is symmetric, this still requires a large number of function evaluations.

2.3. Edge Diffraction

In order to simulate horns with small baffles or flanges, the influence of the pressure diffracted from the edges on the radiation impedance and radiated pressure, must be taken into account. This can be done via the decomposition into three terms of the sound pressure radiated by a monopole, p_0, in a position $\mathbf{x}_0$, on a baffle [28] in $z = 0$,

$$\begin{aligned} p_0(\mathbf{x}) &= p_{IB} + p_{d1} + p_{hod} \\ &= Q\left[G_{IB}(\mathbf{x}|\mathbf{x}_0) + G_{d1}(\mathbf{x}|\mathbf{x}_0) + G_{hod}(\mathbf{x}|\mathbf{x}_0)\right], \end{aligned} \tag{36}$$

where

$$G_{IB} = 2\frac{\mathrm{e}^{-\mathrm{j}kr}}{r}$$

is the infinite-baffle Green's function, for a monopole source signal $Q = \mathrm{j}\omega\rho U/4\pi$, U is the volume velocity and r is the same as in Equation (29). G_{d1} is the corresponding Green's function for the first-order diffraction waves off the edges of the finite baffle, and G_{hod} represents the second and all higher orders of diffraction. For a velocity distribution on a baffle, specified by the volume velocity distribution, $U(x_0, y_0)$, the radiated sound pressure is then given by a surface integration over this velocity distribution,

$$p_{total}(\mathbf{x}) = \frac{\mathrm{j}\omega\rho}{4\pi S}\int_S U(x_0, y_0) \cdot \left[G_{IB}(\mathbf{x}|\mathbf{x}_0) + G_{d1}(\mathbf{x}|\mathbf{x}_0) + G_{hod}(\mathbf{x}|\mathbf{x}_0)\right]\mathrm{d}S_0.$$

The G_{IB}-term yields the Rayleigh integral in Equation (29), so the sound pressure for the finite-baffle case is

$$p_{fb}(\mathbf{x}) = p_{IB}(\mathbf{x}) + \frac{\mathrm{j}\omega\rho}{4\pi S}\int_S U(x_0, y_0) \cdot \left[G_{d1}(\mathbf{x}|\mathbf{x}_0) + G_{hod}(\mathbf{x}|\mathbf{x}_0)\right]\mathrm{d}S_0. \tag{37}$$

A frequency-domain formulation for the first-order diffraction term, G_{d1}, was presented by Svensson *et al.* [29] in the form of a line integral along the edges of a scattering object. An efficient method for computing the resulting integrals was later presented by Asheim and Svensson [30]. The higher-order diffraction term, G_{hod}, can be computed for convex, rigid scattering objects via an integral equation, as shown in [28]. The methods described in these papers are, or will be, implemented in a freely available Matlab toolbox [31].

A modified beta version of this toolbox was used for the computation of edge diffraction effects for the special case of a thin baffle.

3. Computations

The horn used as an example in the computations had the same size and shape as the horn used in the measurements in Section 4. The cross-sectional area follows the hyperbolic-exponential horn profile of Salmon-type horns [32]. The area expansion is given by

$$S(z) = S_{th}\left(\cosh k_c z + T\sinh k_c z\right)^2, \tag{38}$$

where k_c is the cutoff wavenumber, S_{th} is the throat area, and T is a parameter determining the shape of the horn. The horn used in the calculations had $S_{th} = 42.25\,\mathrm{cm}^2$, $S_m = 1188.80\,\mathrm{cm}^2$, $T = 0.7$ and a cutoff frequency of 200 Hz. The length of the horn was 0.5 m. When not placed in a large baffle, the horn was fitted with a 0.5×0.5 m flange.

3.1. Radiation Impedance

Radiation impedance for the infinite baffle case was computed from the equations given by Kemp [20] for the symmetric case, since the horn in question is quarter symmetric.

From the relations in Equations (38) and (35), we see that we can then find the total radiation impedance as

$$Z_{rad,tot} = Z_{IB} + Z_{d1} + Z_{hod}, \tag{39}$$

where Z_{d1} and Z_{hod} are impedances due to the diffracted pressure.

To compute Z_{d1} and Z_{hod}, we must perform the double surface integral of Equation (35) over the horn mouth surface, using the edge diffraction Green's functions G_{d1} and G_{hod}, respectively, from Equation (36). A simplified geometry has been used, where the exterior of the horn is represented only by an infinitely thin plate corresponding to the flange. This simplified geometry reduces both the number of edges that have to be discretized, and the number of paths for higher order diffraction, hence reducing computation time. A grid of 24 by 24 points distributed according to the Gauss-Legendre quadrature rule was placed over the area of the horn mouth on one side of the plate, see Figure 2. Each point was used both as source and as receiver. Since the direct sound is computed separately, no singularity occurs when $\mathbf{x} = \mathbf{x}_0$.

The method to compute G_{hod} encounters singularities when a receiver point, $\mathbf{x}$, in free space is co-planar with the edges. However, for the impedance computation all receiver points are on the baffle, and no such singularity problems occur. A final singularity occurs when $\mathbf{x}$ is very close to an edge, but for the horns studied here, a part of the flange always extends beyond $\mathbf{x}$ and $\mathbf{x}_0$ when calculating the radiation impedance.

The transfer functions between all combinations of sources and receivers were calculated separately. First order and higher order diffraction terms were also kept separate in the calculations, to investigate their effects separately.

When all transfer functions had been computed, the integral of Equation (35) was performed for each combination modes, using the Gauss-Legendre rule. This produced an impedance matrix giving the contribution of the edge diffraction, which was then added to the radiation impedance for a duct in an infinite baffle to produce the total radiation impedance.

3.2. Radiated Pressure

In addition to the surface points, a set of receiver points in front of the horn was also included. The pressures at these points were calculated from (38). The velocity distribution at the mouth was computed with the total radiation impedance taken into account.

For receiver points close to an edge, or near the plane of the flange, the singularities mentioned in Section 3.1 lead to a need for finer discretization. In this study, care has been taken to not place $\mathbf{x}$ too close to any edge, thereby avoiding any extra discretization and increase in computation time.

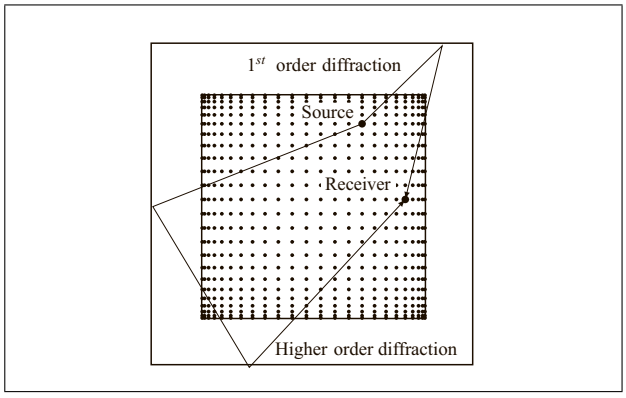

Figure 2. Geometry of horn flange, with the placement of source and receiver points for edge diffraction calculation. Example paths for first order and higher order diffraction are indicated.

3.3. Dependence on Number of Modes in Horn

To evaluate the required number of modes for a given accuracy, calculations for the infinite baffle case with 1, 4, 16, 64 and 256 modes have been performed. To reduce the time required for subsequent computations, the radiation impedance for a fairly large ka range was precomputed, and scaling and interpolation used thereafter.

Results were computed at 200 logarithmically spaced frequencies from 40–6000 Hz. 100 duct elements were used in the MMM simulation of the horn. Accuracy depends on the number of elements, but this is not studied in this paper. The dependence has been studied in [24].

The relative error in throat impedance is calculated as

$$\varepsilon_z = \left| \frac{Z_N - Z_{256}}{Z_{256}} \right|, \tag{40}$$

where Z_N is the throat impedance for N modes, and Z_{256} is the throat impedance from the reference simulation using 256 modes.

Plots of the magnitude of the throat impedance, with 1, 4 and 256 modes, are shown in Figure 3. The curves for 16 and 64 modes are not shown, since they would overlap too much with the curve for 256 modes to be visible. The relative error is plotted in Figure 4. A few observations can be made:

- The error is greatest around the first resonance peak. Inspection of Figure 3 shows that this is to a large degree caused by a shift of the resonance frequency, although for the plane wave simulation ($N_{modes} = 1$), there is also a quite large deviation in amplitude.
- The main contribution of the higher order modes on the throat impedance is to move the resonance peaks to the correct frequencies. This is to a large degree achieved by using just two modes in each direction, with additional modes mainly correcting the amplitude of the peaks.

The mean and maximum errors are given in Table II.

For radiated pressure, the pressure was calculated along two arcs centered at the horn mouth center. The arcs had radii of 0.5 and 3.0 m, respectively. This was to check if

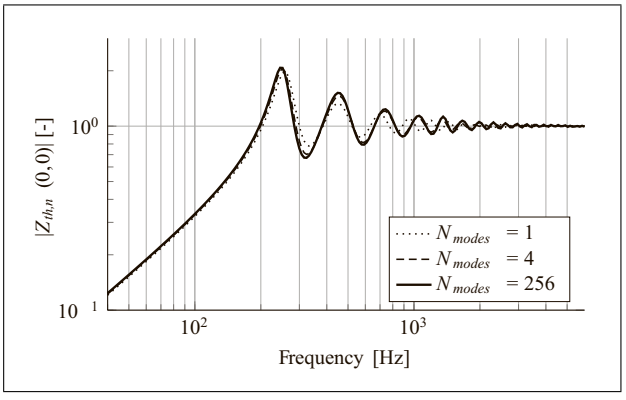

Figure 3. Magnitude of Z_{th} (normalized) for different number of modes.

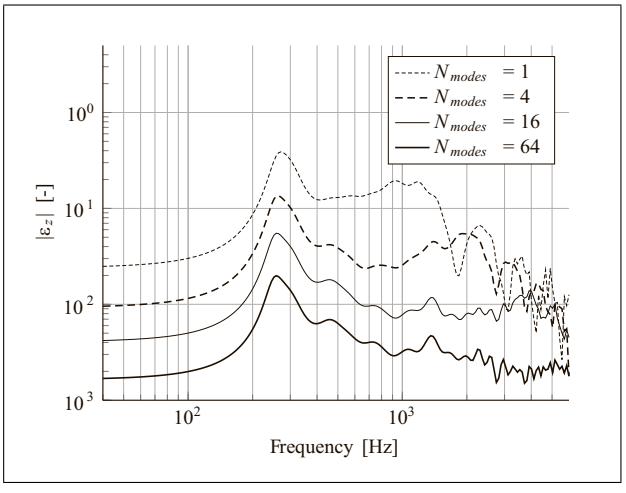

Figure 4. Relative error for Z_{th} for different number of modes.

there was any difference in error between near field and far field calculations. The results are summarized in Tables Table III and Table IV. Here the maximum and mean deviations $\Delta L_p = L_{p,256} - L_{p,N}$ from the reference case are given, in addition to the frequency where the maximum deviation for any field point exceeds 1 dB. Other ways of presenting the differences are given in [24].

One can make the following observations:

- The maximum error can be very large when few modes are used. This is to a large degree due to nulls or near-nulls in the off-axis response for these cases. The errors in the on-axis response are considerably smaller, but still relatively large.
- As more modes are added, the error stays below 1 dB up to higher frequencies.

Judging from the above results, 64 modes would be enough to perform a simulation of this horn to within 1 dB up to around 4600 Hz.

3.4. Dependence on Number of Modes in Diffraction Calculations

The pressure diffracted from the flange edges back into the horn mouth, or into the far field, can also be described by modes. Each mouth velocity mode will produce a different excitation of the edges, and the resulting diffracted pressure will modify both the radiation impedance seen by the horn, and the field point pressure. However, higher order velocity modes usually have both lower amplitude than the plane wave mode, and directivity patterns that might reduce their contribution to the edge terms. Since computing the contribution of the diffracted pressure to the radiation impedance involves the quadruple integral of Figure 35 for each mode, it would be advantageous if the number of modes could be reduced. It is the purpose of this section to investigate the resulting error if only a small number of modes is used to describe the contribution of the diffracted pressure.

Table II. Mean and maximum error for Z_{th}.

N_{modes}	Max$\lvert\varepsilon_Z\rvert$	$\overline{\lvert\varepsilon_Z\rvert}$
1	0.389	0.090
4	0.135	0.031
16	0.055	0.012
64	0.020	0.004

Table III. Error in near field pressure. The number in parenthesis applies to the on-axis pressure.

N_{modes}	Max$\lvert\Delta L_p\rvert$ [dB]	$\overline{\lvert\Delta L_p\rvert}$ [dB]	$f_{\Delta L_p<1\text{dB}}$ [Hz]
1	17.0 (9.1)	1.40 (2.20)	195
4	14.5 (3.4)	0.94 (0.65)	1324
16	13.5 (1.9)	0.46 (0.28)	2459
64	1.74 (0.7)	0.10 (0.10)	4664

Table IV. Error in far field pressure. The number in parenthesis applies to the on-axis pressure.

N_{modes}	Max$\lvert\Delta L_p\rvert$ [dB]	$\overline{\lvert\Delta L_p\rvert}$ [dB]	$f_{\Delta L_p<1\text{dB}}$ [Hz]
1	20.0 (9.20)	1.80 (1.68)	0195
4	22.5 (5.26)	1.10 (0.71)	1358
16	24.0 (2.30)	0.52 (0.29)	2486
64	1.55 (0.88)	0.11 (0.10)	5290

In the following, the simulations were performed with 144 modes. A frequency range of 100 Hz to 2 kHz was used for this study. The diffraction contribution to the radiation impedance was decomposed into a number of modes and added to the modal radiation impedance for an opening in an infinite baffle. For the reference simulation, all 144 modes were used. For other simulations, 144 modes were still used in total, the diffraction contribution is only added up to mode $N_{m,diff}$. I.e. in the 144 × 144 impedance matrix, entries (1,1) to ($N_{m,diff}$, $N_{m,diff}$) contained $Z_{IB} + Z_{d1} + Z_{hod}$, while the other entries only contained Z_{IB}. A test was also done using only the diffraction impedance terms along the diagonal of the impedance matrix, i.e. where a velocity mode couples to a pressure mode of the same shape.

Figure 5 shows the relative error in throat impedance as function of the number of modes included in the diffrac-

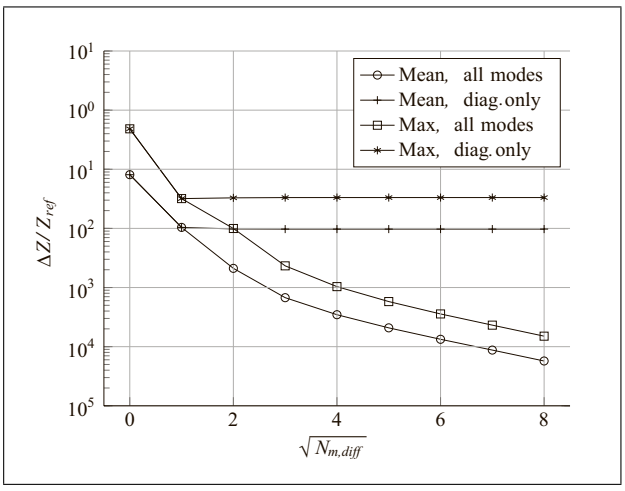

Figure 5. Relative error in Z_{th} as function of number of modes used in the diffraction impedance for the small-flange example. Mean and maximum values have been computed over the 100 Hz to 2 kHz range.

tion contribution. Please note that the values are plotted in terms of $\sqrt{N_{m,diff}}$ to improve readability.

Generally, the error decreases monotonically when more modes are included in the diffraction computation, as expected. A maximum error of 10^{-3} is reached for $N_{m,diff} = 16$. This could suggest that including only 16 of the 144 modes would give quite an adequate accuracy for many purposes, in the frequency range evaluated here, up to 2 kHz. Modal coupling is clearly important, as adding only the diagonal terms does not reduce the error beyond the first mode.

To see the reason for the modal coupling through diffraction, we may inspect the pressure distribution in front of the horn, for three cases: infinite baffle, the diffracted pressure only, and the sum of the two, which corresponds to a horn with a small flange. In the example, the mouth of the horn was given a velocity distribution corresponding to symmetric mode (1,0), which has two minima across the horn mouth in the x-direction. The three cases are plotted in Figure 6, where the pressures along a line across the center of the horn mouth and 1 mm in front of it, are plotted. The horn mouth itself extends from -0.174 m to 0.174 m on the x-axis, indicated by the dash-dotted vertical lines in the figures. In Figures 6a and 6b, it can be seen that the infinite baffle pressure follows the shape of the velocity distribution closely, with minima that move only slowly with frequency. The number of minima inside the horn mouth is the same as for the excitation. This means that the dominant pressure mode is the same as the velocity mode, and the radiation impedance matrix will be diagonally dominant.

The matter is quite different for the diffracted pressure, Figure 6c. Here the number of minima varies strongly with frequency. The radiation impedance matrix due to diffraction will therefore not be diagonally dominant in general.

By comparing the plots in Figure 6, one notices that the magnitude of the diffracted pressure is well below the magnitude of the infinite baffle pressure. At low frequencies, the contribution to the total pressure is negligible, which can be seen by comparing the infinite baffle pressure with the total pressure in Figure 6a. One does, however, notice that the dips at 500 Hz are shallower with diffraction included. One may ask why the contribution of the diffracted pressure seems to be so small, when we know that the effect of diffraction is greatest at low frequencies. A look at the radiation impedance with and without diffraction, Figure 7, may clarify the matter. Although this figure shows the radiation impedance of a piston, the trend is similar for other modes. At low frequencies, the diffraction has very little influence on the reactance, but quite a large influence on the radiation resistance. Since the reactive part of the pressure dominates the near field at these frequencies, and since only the magnitude of the pressure is plotted in Figure 6, the influence of the diffraction seems small.

At middle frequencies, we can see from both Figure 6b and Figure 7 that the contribution of diffraction to the total pressure is greater (600 Hz to 1 kHz curves), until the effect is again negligible at 2 kHz. The larger contribution from diffraction in the 500 Hz to 1 kHz range can also be seen from Figure 6c.

In Figure 6c, for positions close to the baffle edge ($x \approx \pm 0.25$ m), numerical challenges, as described in Section 3.1, lead to reduced accuracy. Therefore, the apparent dip near those baffle edges might be a numerical artifact.

3.5. First Order and Higher Order Diffraction

Usually the most dominant part of the diffracted field comes from the first order diffraction term, as long as the diffracting edge is visible from both the source and the receiver positions. Since computing the higher order diffraction term is time consuming, it is interesting to see how large a contribution this term makes to radiation impedance and radiated pressure. Several simulations were run, where the number of first order diffraction impedance modes (D1ZM), N_{D_1}, was varied from 0 to 64, and the number of higher order diffraction impedance modes (HDZM) was varied from 0 to N_{D_1}. The case of zero diffraction impedance modes corresponds to the infinite baffle case. Otherwise the test was identical to the test in the previous section, including the stepping of N_{D_1} and N_{HOD}.

The results for relative impedance error and relative pressure error are presented in Figures 8 and 9, respectively. Again, the values are plotted against $\sqrt{N_{HOD}}$ to improve readability when N_{HOD} is low, due to the many data points in this region. The trends are similar for both impedance and pressure. It is clear that including only the part of the diffraction pressure that corresponds to a plane piston source, gives a significant reduction in error: the error in impedance is halved if a single D1ZM is included. However, unless higher order diffraction is included, adding more D1ZM has little effect. A further significant reduction of error results by including one or more HDZM. The large reduction in error from no HDZM to a single HDZM

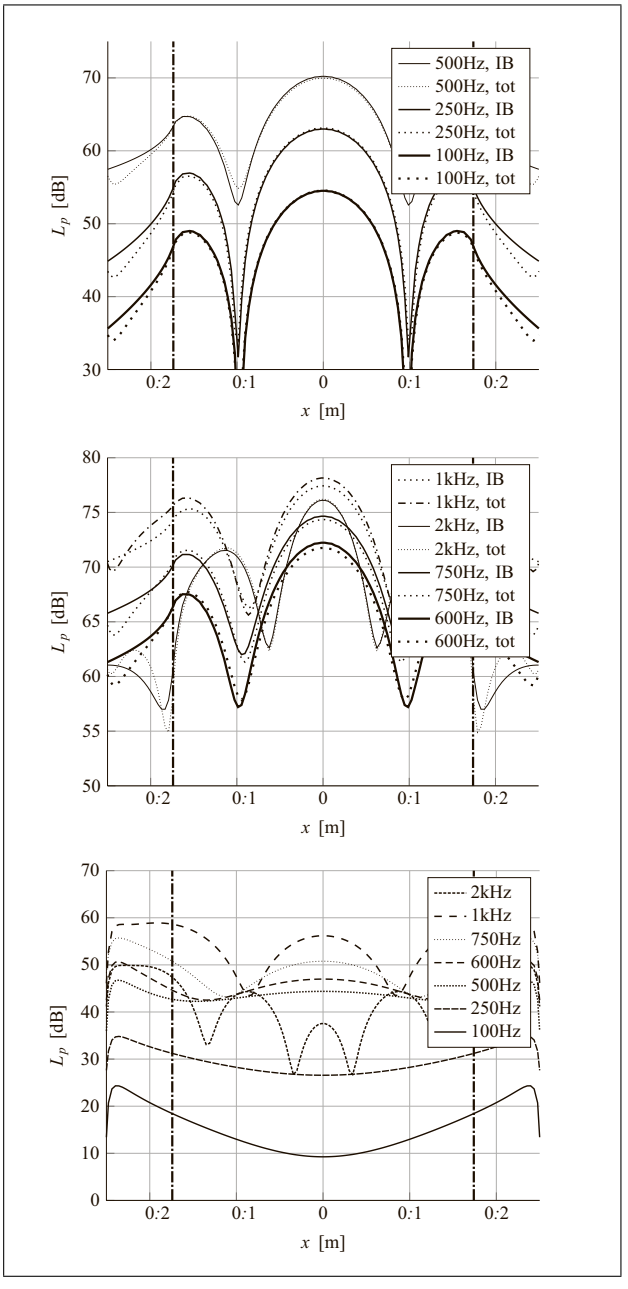

Figure 6. Pressure across horn mouth for velocity mode (1,0). The horn mouth extends between the dash-dotted lines. Please note the different vertical scales. (a) Infinite baffle and total pressure, low frequencies, (b) Infinite baffle and total pressure, middle to high frequencies, (c) Diffraction contribution to pressure.

shows that higher order diffraction is important in establishing the correct zeroth order mode radiation impedance. The influence on the radiation impedance can be seen in Figure 7. The influence is clearly largest for the radiation resistance, the reactance being substantially the same in all three cases.

A reduction of the mean relative error to 0.1% can be achieved with three D1ZM and two HDZM. About 25 to 36 D1ZM and 9 to 16 HDZM are required to reduce the maximum error to the same level.

This distinction between first order and higher order diffraction is largely of academic interest, though, as in

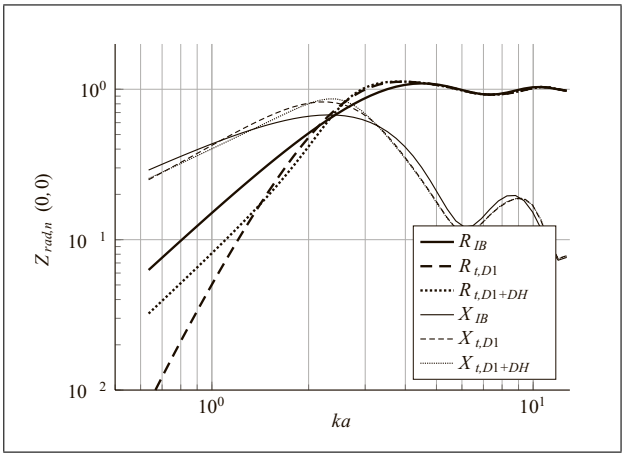

Figure 7. Contribution of higher order diffraction to the fundamental mode radiation impedance.

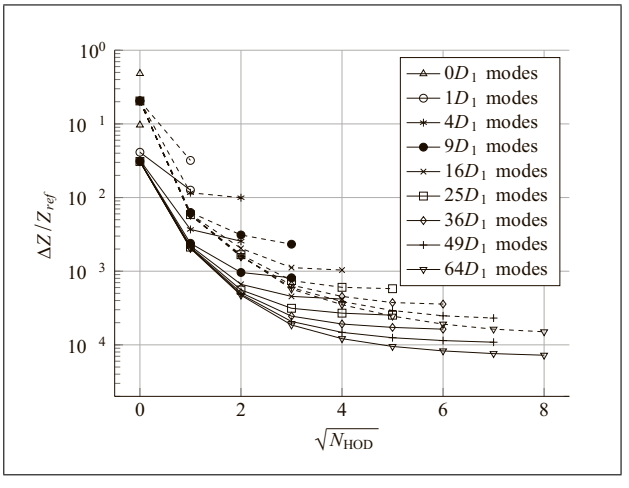

Figure 8. Error in throat impedance as function of number of modes in diffracted pressure. The number of modes in first order diffraction impedance are indicated by the markings on the lines. Solid lines indicate mean error, dashed lines indicate maximum error.

practice the D1ZM and HDZM would not be calculated separately. One would rather calculate the modal diffraction impedances from the total diffracted pressure.

3.6. A Word About Efficiency

The efficiency of the MMM compared to other methods has not been studied in this work, but some comparisons have been made in [24]. It is clear that computational speed depends quite strongly on the number of modes used, and the number of elements in the horn. The number of modes and elements needed depends on the frequency. A larger number of modes is required for good accuracy at higher frequencies, and since many modes will be evanescent in part of the horn, shorter elements are needed to avoid numerical difficulties.

An advantage of the MMM is that the method is scalable; a low number of modes can be used for initial investigations, and more modes added as needed. Another advantage is that no mesh generation is needed, although

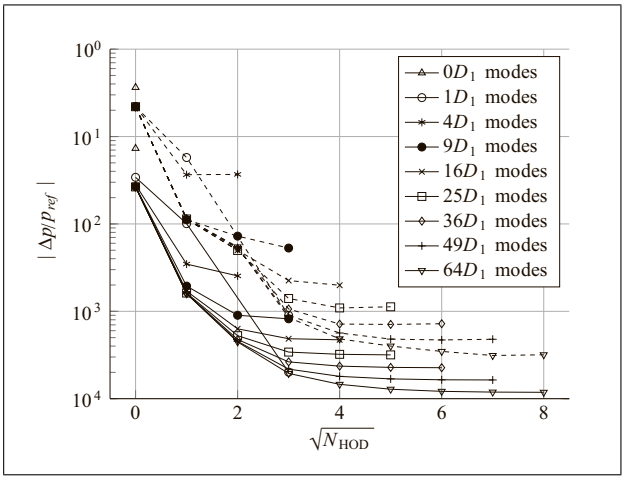

Figure 9. Error in radiated far-field pressure as function of number of modes in diffracted pressure. Legend as in Figure 8.

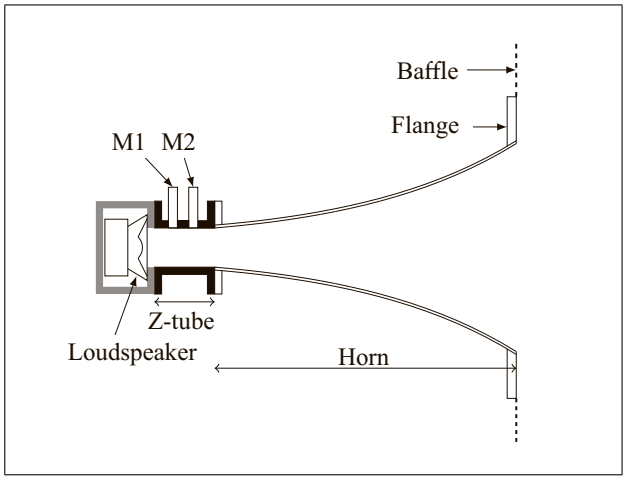

Figure 10. Measurement setup.

this is partially offset by the fact that the allowable geometries are restricted to the ones that can be described as a series of rectangular (or circular) ducts.

For the comparisons in Section 5, reference results have been computed using the Boundary Element Method (BEM) and Boundary Element Rayleigh Integral Method (BERIM). The computer codes for these methods are developed in FORTRAN by Stephen Kirkup [33, 15], but for the current application, the BEM code has been implemented in C++ with OpenMP parallelization. The run time for a mesh of 858 elements was about 20 minutes, compared to 10 minutes for the Matlab implementation of MMM (for 256 modes and 100 duct elements). This does not include the computation of the radiation impedance, which is done in C++/OpenMP and takes another 10 minutes. However, the radiation impedance has to be computed only once for each aspect ratio and tabulated.

The efficiency of the edge diffraction computation is very low in this case, due to the lack of parallelization of the code, and extensive use of nested for-loops, which is detrimental to speed in Matlab. The toolbox, as currently implemented, does not handle a large number of sources efficiently. Run time for the current problem was several hours. Significantly more efficient implementations are anticipated for compiled implementations tailored to the thin baffle case.

In summary, a fair comparison of the efficiency of the various methods would require that the same amount of care and optimization had been applied to all of them, so that each method performed at its best.

Efficiency was however not the main interest in this investigation, but rather to investigate the contribution of diffraction separately from the direct sound. This can hardly be done using conventional element-based methods like BEM.

4. Measurements

A horn of the size and shape described in Section (3) was manufactured using bent MDF sheets with an inner skin of 1 mm aluminium. Total wall thickness was 14 mm, and stiffening ribs were glued to the outside. The horn was fitted with a 0.5 by 0.5 m flange that fitted into a large baffle. Measurements were made of both throat impedance and frequency response at various points in front of the horn, and the radiated pressure was computed in the same positions.

Table V. The mounting arrangements for the two horns. *Offset* is the position of the center of the horn mouth relative to the center of the baffle/flange.

Mounting type	Size [mm]	Offset [mm]
Large baffle	1255 × 1361	(107.5, 81.5)
small flange	500 × 500	(0, 0)

4.1. Setup

The setup is shown in Figure 10. The loudspeaker unit, a SEAS 11F-GX 4" midrange unit, was mounted in a small closed cabinet (grey) filled with acoustic foam. This combination was connected to the horn through a 100 mm long impedance tube (black) in which two Brüel & Kjær 4149 microphones, M1 and M2, were mounted. The loudspeaker was driven by a signal from the WinMLS measurement system through a Lynx sound card and a Quad 50E power amplifier.

The radiated pressure was measured with a Brüel & Kjær 4190 microphone.

Two mountings were used, as indicated in Figure 10, and described in Table V.

All measurements were done in an anechoic chamber.

4.2. Throat Impedance

The throat impedance was measured using the conventional two-microphone method, which is the standard method of measuring the acoustical impedance of absorbing material, mufflers and horns. The method, including the calibration, is described in detail in ISO 10534-2 [34].

It is known that the measurement results become unreliable above the first mode cutoff frequency, and at frequencies where the microphone spacing $\Delta x = n\lambda/2,\ n = 1, 2, \ldots$. The first mode cuts in at about 2.6 kHz, and the microphones are one-half wavelength apart at 5.0 kHz.

It should be noted that the impedance tube is much shorter than the length recommended in the standard, and the distance between the microphone is also small (33.7 mm), considering the low frequencies measured. It has been found, however, that it is still possible to achieve good signal-to-noise ratios down to fairly low frequencies using short impedance tubes [35].

4.3. Frequency Response

The frequency response was measured at several points in front of the horn, both on- and off-axis, with the impedance tube in place. Measurements were done relatively close to the horn, compared to typical directivity measurements. The purpose of the measurements was, however, the comparison with simulations, and the simulations should be valid for all distances.

5. Comparisons

In this section, comparisons of measured and simulated values will be given. The measurements were compared to both the MMM, MMM with Edge Diffraction (MMM + ED), and two Boundary Element Methods (BEM). For the flanged horn, ordinary BEM was used [33], with a simple pyramid-shaped enclosure around the horn, see Figure 11. A simplified geometry was used to avoid discretizing the thin flange and the many small details on the outside of the actual horn. Discretizing these thin objects would result in many small surface elements and extended computation time, without giving any clear benefit.

For the baffled horn, the Boundary Element Rayleigh Integral Method (BERIM) [15] was used. BERIM combines the Boundary Element Method for the interior of the horn with a Rayleigh integral formulation for the exterior. This method is ideal for simulating horns mounted in large/infinite baffles. An infinite baffle was also assumed in MMM simulation of the baffled horn, i.e. the large but finite baffle was treated as an infinite baffle in the simulations.

The influence of edge diffraction was calculated for the frequency range 100 Hz–2 kHz. Extrapolation of the data was used below this range, but above 2 kHz the diffraction contribution was ignored.

5.1. Throat Impedance

The throat impedance for the test horn mounted in a large baffle is shown in Figure 12. Measurements (solid lines) are compared to MMM (dashed) and BERIM (dotted)[4].

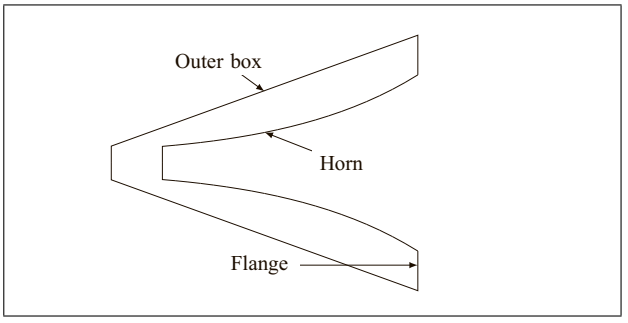

Figure 11. BEM geometry for the horn with flange.

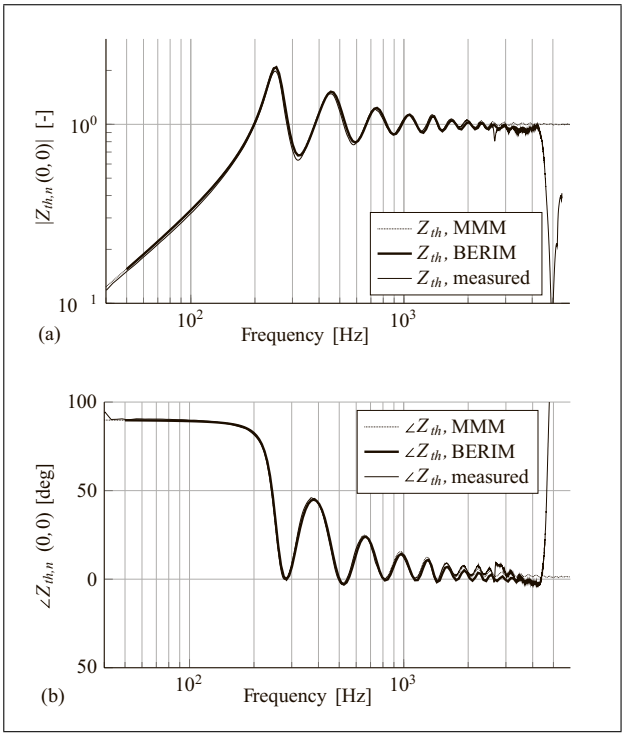

Figure 12. Throat impedance for the test horn in a large/infinite baffle. (a) Magnitude (normalized), (b) Phase.

The introduction of the first mode in the measurement setup at approx. 2.6 kHz can be seen, and one notices the increased deviation from the simulated values above this frequency. The measurements break down completely above approximately 4.2 kHz, as opposed to the theoretical 5 kHz. This is, however, most likely due to the finite dimensions of the 0.5" microphones, since the 33.7 mm distance is the center-center spacing.

256 modes were used in this simulation, and the horn consisted of 100 duct sections. For the BERIM simulation, a mesh bandwidth[5] of 3 kHz has been used, and the symmetry of the geometry was exploited.

[4] In the BERIM and BEM simulations, the magnitude of the impedance does not completely reach the asymptotic ρc impedance value unless the mesh is very fine. This may be related to the collocation used in the method, or to numerical dispersion as discussed by Bängtson *et al.* [36]. It has been found necessary to increase the impedance by an empirical factor of 4.2% to compensate for this.

[5] The mesh bandwidth is understood as the frequency where the largest element of the mesh is not larger than $^1/_6$th of a wavelength.

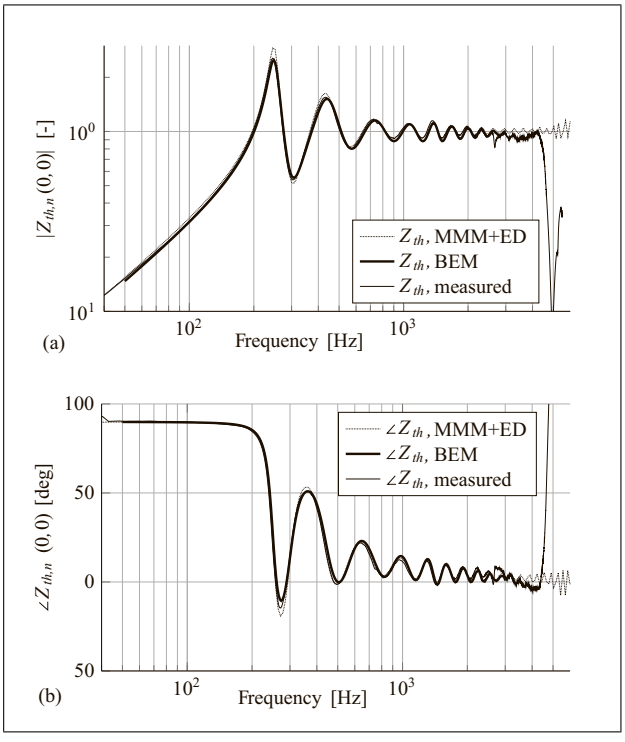

Figure 13. Throat impedance for the test horn with a small flange. (a) Magnitude (normalized), (b) Phase.

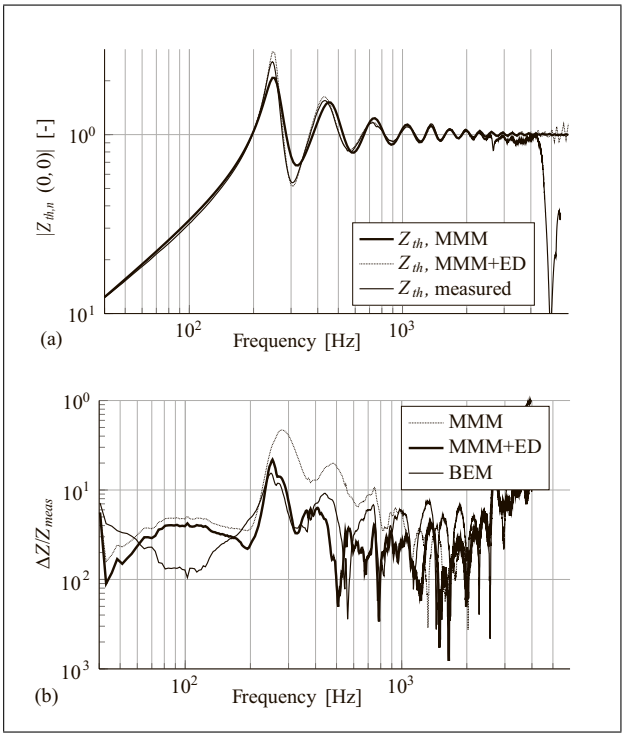

Figure 14. MMM simulations compared to measured throat impedance for the test horn with a small flange, with and without edge diffraction. (a) Magnitude, (b) Relative difference.

The throat impedance for the test horn with the small flange, is shown in Figure 13. Again, increased deviation above 2.6 kHz can be seen. 196 modes have been used for the simulation, as the modal decomposition of

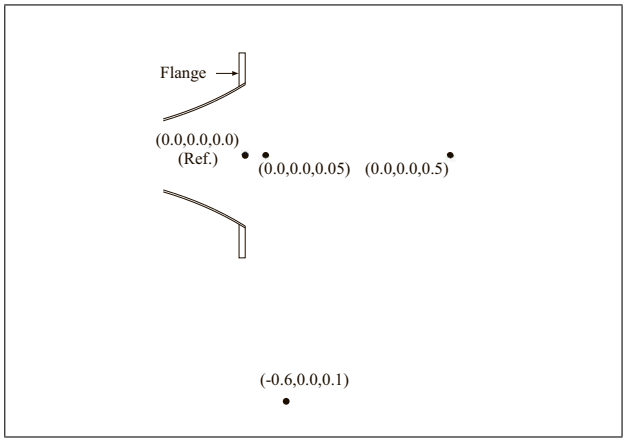

Figure 15. Placement of field points. Units in meters.

the diffraction-related radiation impedance with the given number of integration points did not allow for modes of higher order to be reliably resolved. As in the large/infinite baffle case, the horn consisted of 100 duct elements. For the BEM simulation, a mesh bandwidth of 2 kHz was used, and the symmetry of the geometry was exploited. The geometry used is illustrated in Figure 11.

As expected, the impedance ripple is higher for the horn with a flange than for the horn in the large baffle. This is mainly due to the reduced value of the radiation impedance at low frequencies for the flanged case, see Figure 7. The MMM+ED overestimates the first impedance peaks somewhat. The most likely reason for this is that the geometry of the horn is approximated by a single thin plate representing the flange, and the rear side of the horn is ignored.

In Figure 14a the measured throat impedance for the flanged horn is compared to simulations using MMM and MMM+ED. In Figure 14b the relative error is shown for the two cases, in addition to the BEM simulation. For this figure, the simulated impedance values have been interpolated to the frequency values in the measurements, before computing the error.

The following observations can be made:

- If the baffle is "large enough", it behaves like an infinite baffle.
- The effects of a small flange or baffle, cannot be ignored. Simulating the horn as if it was mounted in an infinite baffle gives large errors at low to medium frequencies.
- Part of this error comes from a frequency shift of the resonance peaks, but also from predicting the wrong amplitude of those peaks.
- The error using MMM with edge diffraction reduces the error to below 5% for most of the frequency range. This is actually better than BEM over much of this range, although this could probably be improved by using a finer mesh.

5.2. Radiated Pressure

To make comparisons between simulations and measurements that are relatively independent of the behavior of the

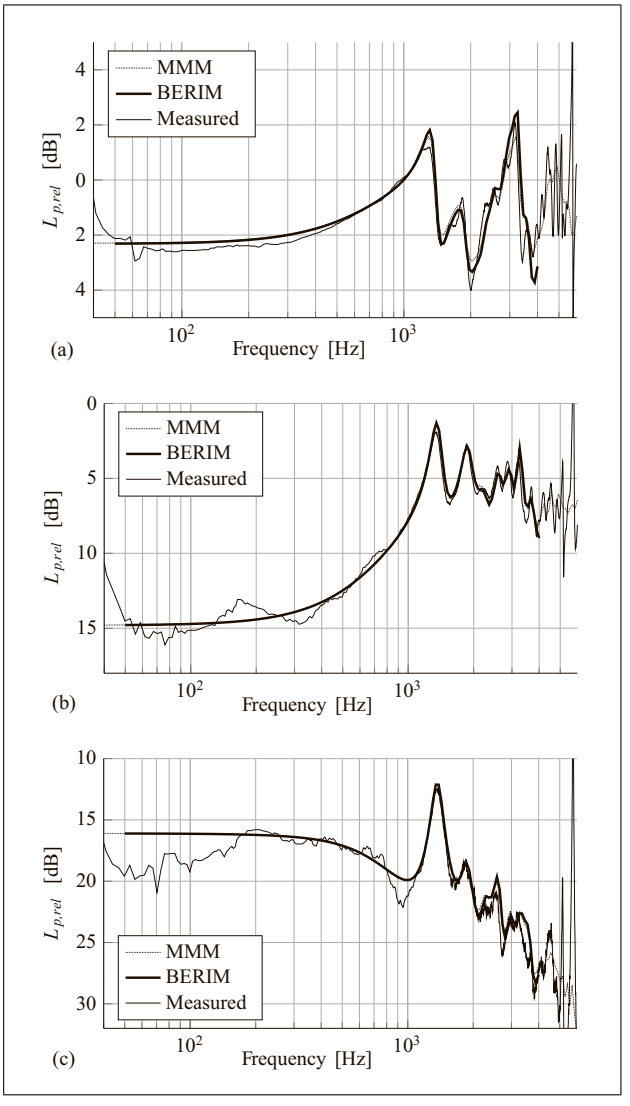

Figure 16. Radiated pressure for the test horn in a large baffle.
(a) $p(0.0, 0.0, 0.05)/p(0.0, 0.0, 0.0)$,
(b) $p(0.0, 0.0, 0.5)/p(0.0, 0.0, 0.0)$,
(c) $p(0.0, 0.0, 0.1)/p(0.0, 0.0, 0.0)$.

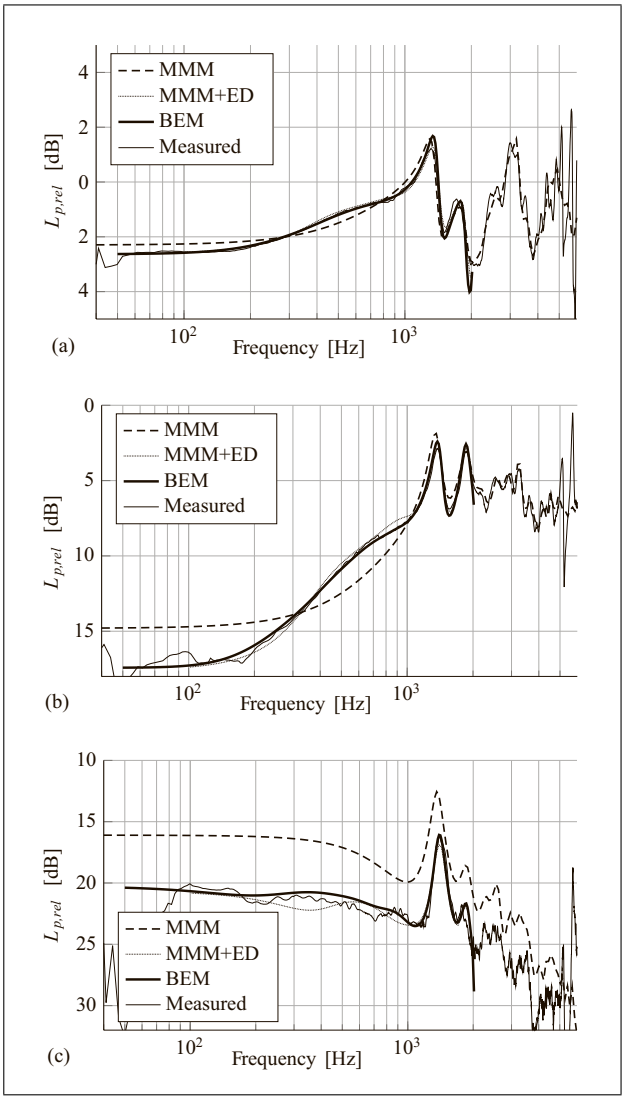

Figure 17. Radiated pressure for the test horn with a small flange.
(a) $p(0.0, 0.0, 0.05)/p(0.0, 0.0, 0.0)$,
(b) $p(0.0, 0.0, 0.5)/p(0.0, 0.0, 0.0)$,
(c) $p(0.0, 0.0, 0.1)/p(0.0, 0.0, 0.0)$.

loudspeaker driver used, a point at the center of the horn mouth has been used as reference. This point has been designated as the origin, and the pressures at all other points are compared to the pressure here. See Figure 15.

Figure 16 shows the relative responses at three different points in front of the baffled horn: one very close, one at a distance on the principal axis, and one that is out to the side and fairly close to the plane of the baffle. It can be seen that the MMM and BERIM simulations follow each other well, and both capture the principal features of the measurements. The deviation at low frequencies is most likely due to the influence of the finite baffle used in the measurements. This is also most likely the cause of the deviation at 1kHz in Figure 16c, since this point is quite close to the baffle edge.

Figure 17 shows the response at the same points in front of the horn with a small flange. Again, both MMM+ED and BEM capture the principal features of the measurements. Above 2kHz the BEM simulation experiences problems with eigenfrequencies, so results for frequencies above 2kHz are not shown. Since the edge diffraction terms are only calculated in the range 100Hz to 2kHz, only this range is shown for MMM+ED. The deviation of the MMM+ED results in the 200–600Hz range in Figure 17c could be due to the approximate geometry used in the edge diffraction simulation, since at this point the rear of the horn is visible from the receiver position.

Figure 18 summarizes the responses computed with MMM, MMM+ED and BEM, relative to the measurements for the horn with a small flange. Also here, the simulated values have been interpolated to match the frequencies in the measurements.

It is clear from these comparisons that

- Close to the horn mouth (Figures 17a and 18a) the contribution from edge diffraction is small, even at low frequencies, since the direct sound is strong there. Still,

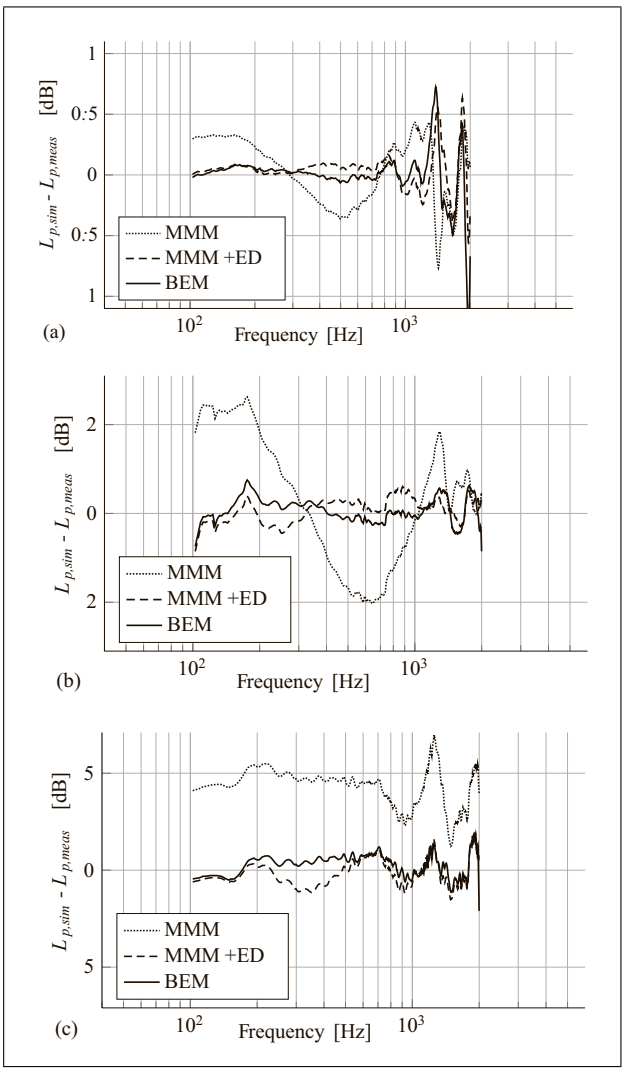

Figure 18. Relative error in radiated pressure for the test horn with a small flange. Please note the different vertical scales.
(a) $p(0.0, 0.0, 0.05)/p(0.0, 0.0, 0.0)$,
(b) $p(0.0, 0.0, 0.5)/p(0.0, 0.0, 0.0)$,
(c) $p(0.0, 0.0, 0.1)/p(0.0, 0.0, 0.0)$.

the methods that take the finite size of the baffle into account (MMM+ED, BEM) are more accurate.

- On-axis, but further from the horn mouth (Figures 17b and 18b), edge diffraction contributes significantly below 1 kHz, but above this frequency the difference between a finite and infinite baffle is small. The reason for this is most likely the directivity of the horn.
- Off-axis (Figures 17c and 18c), the edge diffraction alters the directivity pattern significantly over a large frequency range, causing large errors at all frequencies for the MMM without ED. The difference between the MMM+ED and BEM results are probably due to the different geometries for the two methods.

6. Conclusions

By expressing the sound field in a horn as a sum of eigenmodes, the throat impedance and radiated pressure from a loudspeaker horn can be computed with good accuracy. This paper has demonstrated that the method captures the principal features of the radiated pressure when compared to measurements. The method also compares well with other numerical methods, such as the Boundary Element Method and the Boundary Element Rayleigh Integral method. Throat impedance is also computed with good accuracy, enabling accurate computation of radiated power.

The addition of edge diffraction calculations has enabled the method to be used also for horns with small baffles or flanges, and the results compare well with the measurements.

It has been demonstrated that inclusion of the edge diffraction for both computation of the throat impedance and the radiated pressure is required for good accuracy. There will be large errors, especially at low frequencies and large off-axis angles, if the finite baffle size is not taken into account.

Acknowledgment

The authors wish to acknowledge Tore Landsem and Tore Berg at the workshop at IET, NTNU, for building the horn used in the experiments. The horn held the specified dimensions with a tolerance better than 1%.

References

[1] A. G. Webster: Acoustical Impedance and the Theory of Horns and of the Phonograph. Proc. Nat. Ac. Sci. **5** (Jul 1919) 275–282.

[2] E. Eisner: Complete Solutions of the Webster Horn Equation. J. Acoust. Soc. Am. **41** (1966) 1126–1146.

[3] D. P. Berners, J. O. Smith III: Super-Spherical Wave Simulation in Flaring Horns. Proceedings of the International Computer Music Conference (1995).

[4] D. P. Berners: Acoustics and Signal Processing Techniques for Physical Modeling of Brass Instruments. Dissertation. Stanford University, 1999.

[5] T. Hélie: Unidimensional models of acoustic propagation in axisymmetric waveguides. J. Acoust. Soc. Am. **114** (Nov 2003) 2633–2647.

[6] J. Agullo, A. Barjau, D. H. Keefe: Acoustic Propagation in Flaring, Axisymmetric Horns: I. A New Family of Unidimensional Solutions. Acta Acustica united with Acustica **85** (1999) 278–284.

[7] P. Eveno, J.-P. Dalmont, R. Caussé, J. Gilbert: Wave propagation and radiation in a horn: Comparisons between models and measurements. Acta Acustica united with Acustica **98** (2012) 158–165.

[8] T. Hélie, T. Hézard, R. Mignot, D. Matignon: One-dimensional acoustic models of horns and comparison with measurements. Acta Acustica united with Acustica **99** (2013) 960–974.

[9] K. R. Holland, F. J. Fahy, C. L. Morfey: Prediction and Measurement of the One-Parameter Behavior of Horns. J. Audio Eng. Soc. **37** (May 1991) 315–337.

[10] E. R. Geddes: Acoustic Waveguide Theory. J. Audio Eng. Soc. **37** (Jul/Aug 1989) 554–569.

[11] G. R. Putland: Every One-Parameter Acoustic Field Obeys Webster's Horn Equation. J. Audio Eng. Soc. **41** (Jun 1993) 435–451.

[12] C. A. Henricksen, M. S. Ureda: The Manta-Ray Horns. J. Audio Eng. Soc. **26** (Sep 1978) 629–634.

[13] S. Morita, N. Kyono, S. Sakai, T. Yamabuchi, Y. Kagawa: Acoustic Radiation of a Horn Loudspeaker by the Finite Element Method – A Consideration of the Acoustic Characteristic of Horns. J. Audio Eng. Soc. **28** (Jul/Aug 1980) 482–489.

[14] N. Kyouno, S. Sakai, S. Morita, T. Yamabuchi, Y. Kagawa: Acoustic Radiation of a Horn Loudspeaker by the Finite Element Method – Acoustic Characteristics of a Horn Loudspeaker with an Elastic Diaphragm. 69th Convention of the Audio Engineering Society (May 1981). Preprint no. 1756.

[15] S. M. Kirkup, A. Thompson, B. Kolbrek, J. Yazdani: Simulation of the Acoustic Field of a Horn Loudspeaker By the Boundary Element-Rayleigh Integral Method. Journal of Computational Acoustics **21** (2013).

[16] R. J. Alfredson: The Propagation of Sound in a Circular Duct of Continuously Varying Cross-Sectional Area. J. Sound Vibr. **23** (1972) 433–442.

[17] T. Shindo, T. Yoshioka, K. Fukuyama: Calculation of Sound Radiation from an Unbaffled, Rectangular-Cross-Section Horn Loudspeaker Using Combined Analytical and Boundary-Element Methods. J. Audio Eng. Soc. **38** (May 1990) 340–349.

[18] A. Schuhmacher, K. B. Rasmussen: Modelling of horn-type loudspeakers for outdoor sound reinforcement systems. Applied Acoustics **56** (1999) 25–37.

[19] V. Pagneux, N. Amir, J. Kergomard: A study of wave propagation in varying cross-section waveguides by modal decomposition. Part I. Theory and validation. J. Acoust. Soc. Am. **100** (Oct 1996) 2034–2048.

[20] J. A. Kemp: Theoretical and experimental study of wave propagation in brass musical instruments. Dissertation. University of Edinburgh, 2002.

[21] N. Amir, V. Pagneux, J. Kergomard: A study of wave propagation in varying cross-section waveguides by modal decomposition. Part II. Resuit. J. Acoust. Soc. Am. **101** (May 1997) 2504–2517.

[22] P. M. Morse, U. Ingard: Theoretical Acoustics. McGraw-Hill, 1986.

[23] A. D. Pierce: Acoustics. Acoustical Society of America, 1994.

[24] B. Kolbrek: Modal sound propagation in curved horns of rectangular cross-section. Diploma Thesis. Norges teknisk-naturvitenskapelige universitet, Institutt for elektronikk og telekommunikasjon, Trondheim, Norway, 2013.

[25] J. Jurkiewicz, A. Snakowska, D. Smolik: Acoustic impedance of outlet of a hard-walled unbaffled cylindrical duct for multimode incident wave. Acta Physica Polonica A **119** (2011) 1061–1067.

[26] W. E. Zorumski: Generalized radiation impedances and reflection coefficients of circular and annular ducts. J. Acoust. Soc. Am. **54** (1973) 1667–1673.

[27] J. A. Kemp: Multimodal radiation impedance of a rectangular duct terminated in an infinite baffle. Acta Acustica united with Acustica **87** (Jan/Feb 2001) 11–15.

[28] A. Asheim, U. P. Svensson: An integral equation formulation for the diffraction from convex plates and polyhedra. J. Acoust. Soc. Am. **133** (Jun 2013) 3681–3691.

[29] U. P. Svensson, P. Calamia, S. Nakanishi: Frequency-domain edge diffraction for finite and infinite edges. Acta Acustica united with Acustica **95** (2009) 568–572.

[30] A. Asheim, U. P. Svensson: Efficient evaluation of edge diffraction integrals using the numerical method of steepest descent. J. Acoust. Soc. Am. **128** (Oct 2010) 1590–1597.

[31] U. P. Svensson: Edge diffraction toolbox for matlab. 2013.

[32] V. Salmon: A New Family of Horns. J. Acoust. Soc. Am. **17** (Jan 1946) 212–218.

[33] S. Kirkup: The boundary element method in acoustics. 2nd ed. ed. Integrated Sound Software, 2007.

[34] ISO-10534-2:1998(e): Acoustics – Determination of sound absorption coefficient and impedance in impedance tubes – Part 2: Transfer-function method. 11 1998.

[35] J. T. Post, E. T. Hixon: A Modeling and Measurement Study of Acoustic Horns. Dissertation. University of Texas, May 1994.

[36] E. Bängtson, D. Noreland, M. Berggren: Shape optimization of an acoustic horn. Computer Methods in Applied Mechanics and Engineering **192** (2003) 1533 – 1571.